Heterogeneous Silicon/III–V Semiconductor Optical Amplifiers

Michael L. Davenport, *Student Member, IEEE*, Sandra Skendžić, Nicolas Volet, Jared C. Hulme, *Student Member, IEEE*, Martijn J. R. Heck, *Member, IEEE*, and John E. Bowers, *Fellow, IEEE*

(Invited Paper)

***Abstract*—We report high output power and high-gain semiconductor optical amplifiers integrated on a heterogeneous silicon/III–V photonics platform. The devices produce 25 dB of unsaturated gain for the highest gain design, and 14 dBm of saturated output power for the highest output power design. The amplifier structure is also suitable for lasers, and can be readily integrated with a multitude of silicon photonic circuit components. These devices are useful for a wide range of photonic integrated circuits. We show a design method for optimizing the amplifier for the desired characteristics. The amplifier incorporates a low loss and low reflection transition between the heterogeneous active region and a silicon waveguide, and we report transition loss below 1 dB across the entire measurement range and parasitic reflection coefficient from the transition below $1 \cdot 10^{-3}$.**

***Index Terms*—Semiconductor optical amplifiers, integrated optoelectronics.**

I. Introduction

SILICON (Si) photonics has emerged as a viable technology for metro and short reach data transmission applications due to the potential for high volume and low cost manufacturing that can leverage existing CMOS manufacturing and packaging technologies [1]. A wide range of silicon-on-insulator (SOI) based photonic functions have been demonstrated, such as low-loss vertical and edge couplers to fiber optics, polarization splitting and rotation, and high speed modulators and photodetectors. More recently, the addition of III-V semiconductor material, particularly indium phosphide (InP), to SOI wafers through heterogeneous integration has expanded the suite of components to include lasers, amplifiers, electro-absorption and electro-optic modulators, and high power photodetectors [2].

The scale of Si photonic integrated circuits (PICs) is rapidly increasing, with a recent demonstration of a vertically emitting beam forming chip with 4096 components eclipsing the largest published monolithic InP-based PICs [7]. The progression of the scale of Si photonics PICs compared that of the InP platform is shown in Fig. 1.

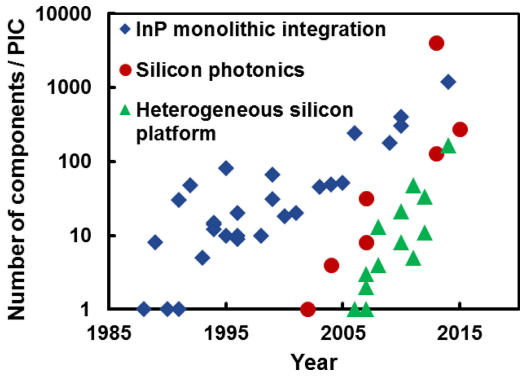

Fig. 1. Increase in the scale of PICs over time. InP data is taken from [3]. Heterogeneous silicon data (green) taken from [2], [4]. Silicon data taken from [5]–[7].

The semiconductor optical amplifier (SOA) will become a critical component for many kinds of PICs to increase output power and maintain signal levels as the signal propagates throughout a large number of optical components. A prominent example is a vertically emitting beam steering chip [4], which splits an integrated laser into 32 channels and uses a carrier-plasma-effect phase tuner to adjust the phase in each channel, which introduces additional loss. An SOA can be used in each channel to compensate for the loss in the splitter and tuner, and also to balance the amplitude profile. This type of PIC requires amplifiers with high gain and high output power, as the power demand is very high in vertical beam-steering applications, such as free-space optical communications [8].

In addition to use in beam steering, SOAs have many other applications in PICs. Widely-tunable lasers for wavelength-division multiplexing (WDM) transmission typically include an integrated SOA to allow optimization of the laser wavelength and side-mode suppression ratio (SMSR) separately from the laser output power [9]. Output optical power requirements for lasers in coherent transmission systems are typically very high, at least 16 dBm, to overcome loss in the coherent modulator, wavelength division multiplexer, and fiber coupling. Fixed multi-wavelength laser arrays may use an SOA after each laser to maintain channel equalization before wavelength multiplexing [10]. Integrated WDM receiver circuits may use an SOA to

Manuscript received February 19, 2016; revised June 24, 2016; accepted July 3, 2016. Date of publication July 19, 2016; date of current version November 9, 2016. This work was supported by the Defense Advanced Research Projects Agency under the DODOS project, Contract number HR0011-15-C-055. The work of N. Volet was supported by the Swiss National Science Foundation.

M. L. Davenport, N. Volet, J. C. Hulme, and J. E. Bowers are with the University of California, Santa Barbara, CA 93106 USA (e-mail: mld01@umail.ucsb.edu; volet@ece.ucsb.edu; jaredhulme@ece.ucsb.edu; bowers@ece.ucsb.edu).

S. Skendžić was with the University of California, Santa Barbara, CA 93106 USA. She is now with the Ultra Communications, Inc.Vista, CA 92081 USA (e-mail: sskendzic@gmail.com).

M. J. R. Heck was with the University of California, Santa Barbara, CA 93106 USA. He is now with the Aarhus University, Aarhus DK-8200, Denmark (e-mail: mheck@eng.au.dk).

Color versions of one or more of the figures in this paper are available online at http://ieeexplore.ieee.org.

Digital Object Identifier 10.1109/JSTQE.2016.2593103

amplify an incoming signal to reduce the number of external optical amplifiers in the network [11]. SOAs can also be used in high-speed wavelength conversion [12] through nonlinear effects such as cross gain modulation.

Figures of merit for SOAs include the unsaturated gain factor G_0, which is the ratio of the output power to the input power, the input saturation power $P_{\mathrm{in},s}$, which is the input power level at which the gain has been reduced to half of its unsaturated value, and the noise figure, which is the degradation in signal-to-noise ratio (SNR) after amplification. At the wavelength of maximum optical gain, the SOA gain factor *G* varies with the input power P_{in} as:

$$G = G_0 \frac{1 + P_{\mathrm{in}}/P_s}{1 + G_0 P_{\mathrm{in}}/P_s}, \tag{1}$$

where P_s is the material gain saturation power. It can be seen from (1) that *G* will decrease with increasing P_{in}, eventually approaching 1 when $P_{\mathrm{in}} \gg P_s$. The relation between the input saturation power $P_{\mathrm{in},s}$ and P_s is described by:

$$P_{\mathrm{in},s} = \frac{P_s}{G_0 - 2}. \tag{2}$$

The saturation characteristic of the amplifier can drastically reduce the gain if the input power is too high. The material gain saturation power can be derived from the laser rate equations, and is equal to:

$$P_s = \frac{hc}{\Gamma_{\mathrm{xy}}} \frac{\sigma_{\mathrm{xy}}}{a\tau\lambda}, \tag{3}$$

where σ_{xy} is the quantum well cross sectional area, λ is the photon wavelength, *a* is the differential gain, Γ_{xy} is the modal overlap with the pumped region of the quantum well, τ is the carrier lifetime, *h* is Planck's constant, and *c* is the speed of light in vacuum. Reducing *a* and τ increases the input saturation power, and this can be accomplished by operating the device at high carrier density. Reducing Γ_{xy} increases $P_{\mathrm{in},s}$, but also reduces G_0. A reduction in the number of quantum wells reduces the cross-sectional area *A*, which reduces P_s, but it also reduces Γ_{xy} and increase the carrier density at a given current bias, for a net increase in P_s. Taking this measure reduces the modal gain coefficient, unfortunately, so the tradeoff between gain and saturation power must be considered carefully for the design of the amplifier.

II. Review

Demonstrations of heterogeneous Si/III-V devices fall broadly into two categories: those directly bonded to Si, and those bonded to a planarizing interlayer, such as the polymer divinylsiloxane-bis-benzocyclobutene (DVS-BCB) or polished silicon dioxide (SiO_2) [13]. Directly bonded devices may be bonded through a hydrophobic process, sometimes referred to as wafer fusion, allowing for conduction through the layers [14], or by hydrophilic bonding, which utilizes a thin oxide layer, normally only a few nanometers thick, to attach the heterogeneous materials [15]. Low temperature hydrophilic bonding is typically accomplished with an oxygen plasma activation to form the thin oxide layer, and allows bonding of materials with larger mismatch of the coefficient of thermal expansion. This method is widely used since InP and Si have a considerable mismatch in their coefficients of thermal expansion. For comparison, hydrophobic bonding in [14] required a bonding anneal temperature of 650 °C, while hydrophilic bonding of InP to Si is normally conducted at 300 °C. Bonding with DVS-BCB can also be conducted at low temperatures, such as 280 °C [16]. High process temperatures can degrade Si/III-V light emitting devices rapidly, except in the case of thin films [17].

In directly bonded devices, the III-V mesa is normally very wide, with the index guiding provided by the immediately adjacent Si waveguide and the current confinement provided by hydrogen implantation [18] of the outsides of the mesa. These function in a similar manner to a shallow-ridge waveguide, and provide most of their amplification to the fundamental mode due to the higher order modes being mainly confined outside of the central current channel. Narrow index-guided III-V mesas which are directly bonded suffer from higher order modes which have high confinement factor, while wide implanted mesa design suffers from the drawback of lower confinement factor in the quantum well. Confinement factors above 1% per well are difficult to achieve. Wide implanted mesas have the advantage of improved thermal conductivity, since the un-pumped sides of the mesa act as heat sinks and have more contact with the relatively more thermally conductive Si. Despite the addition of the highly thermally insulating buried oxide layer, directly bonded hydrogen implanted wide mesa lasers with single transverse mode operation have demonstrated thermal conductivities comparable to native substrate InP lasers [19].

Interlayer bonded lasers normally have a thin interlayer with a low index of refraction, normally SiO_2 ($n = 1.45$) or DVS-BCB ($n = 1.53$). The interlayer serves the purpose of planarizing the Si wafer surface, allowing mechanically robust III-V ridge waveguides with no Si waveguide underneath. This is more difficult in directly bonded devices and makes achieving single transverse mode devices easier, since the overall height of the waveguide core is reduced. Since the optical mode then has no overlap with the Si waveguide, higher confinement factor in the quantum wells can be attained. Up to 1.6% per well has been demonstrated [20], which is advantageous for compact high single-pass gain SOAs. However, the common interlayer materials have poor thermal conductivity, and these types of devices must rely on the III-V waveguide to achieve single transverse mode operation. The narrow waveguide combined with the interlayer and buried oxide can result in high thermal impedance and limit maximum operating current. In addition, the decoupling effect of the interlayer can complicate the transition between the III-V active region and a passive waveguide, although recent publications have shown that this limitation can be overcome with very thin interlayer thicknesses and achieve high performance devices [16], [21].

The earliest work on Si/III-V SOAs, in 2007, was of the directly bonded type [22], using a 14-μm-wide InP mesa and 4-μm-wide current channel defined by hydrogen implantation. The device had angled and anti-reflection (AR) coated polished heterogeneous facets. The amplifier used 8 InGaAlAs quantum wells and a 2-μm-wide Si waveguide, resulting in a relatively

low 3% confinement factor. The device was 1.36 mm in length, and achieved a maximum on-chip gain of 9.1 dB/mm. The input saturation power was reported to be −2 dBm. This was followed by a more advanced version featuring a tapered mode converter for integration with passive waveguides and a photodetector to form a preamplified receiver [23].

An example of an interlayer bonded SOA followed in 2012, using BCB as the interlayer [24]. The device consisted of a narrow 3-μm-wide III-V ridge with 6 InGaAsP quantum wells, coupled to Si waveguides and vertical grating couplers at the input and output with adiabatic couplers [19], [20]. Devices with overall length (including the tapers) of 600 μm demonstrated an on-chip gain of 13 dB, or 21.7 dB/mm, at only 40 mA of drive current. This improvement over the directly bonded amplifier in [23] is due to the increased confinement factor allowed by this device architecture.

In 2014, another interlayer bonded device using SiO_2 for the interlayer was reported [20]. This device was similar in structure to [24] in that it used a narrow III-V ridge and adiabatic couplers. It used a 1100-μm-long amplifier section, and was fully packaged with fibers attached to the vertical grating couplers. This device exhibited 28 dB of on-chip gain, corresponding to 25.5 dB/mm of gain per length. It also demonstrated 10 dB of fiber-to-fiber gain, which is the highest demonstrated value for that figure of merit published to date. The maximum on-chip input saturation power was −16 dBm.

A more recent result, published in 2015 [27] demonstrated high wallplug efficiency using a directly-bonded SOA. The device employed a 75-μm-wide proton implanted III-V mesa, and 3 InGaAlAs quantum wells. The device provided 7.5 dB of gain, or 12.6 dB/mm, considering the device's 600 μm total length. Although the saturation characteristics were not reported, there was little difference in the gain for an input power of −10 dBm (7.5 dB of gain) and 3 dBm of input power (7.1 dB of gain), so it appears that the maximum output power could be considerably higher than the previously reported SOAs. An amplifier with a flared Si waveguide was demonstrated, and due to the excellent low resistance electrical characteristics of the amplifier, it displayed a very high wallplug efficiency of 12.1%.

A summary of the existing heterogeneous Si/III-V SOAs is shown in Table II, along with the two best performing devices from this work and a commercially available InP substrate SOA.

III. Waveguide Design

The configuration of the III-V layers must be carefully considered for use in a heterogeneous amplifier. Many elements of the design can be copied from monolithic III-V amplifiers. However, the effect of the Si waveguide on the optical mode and the inability to extract current through the bonded region with the present level of technology requires modification to the design of the epitaxial layers.

The design of the quantum wells and barriers is unaffected by heterogeneous integration, and can be copied from an existing monolithic design or design methodology. This subject is covered in more detail in [28].

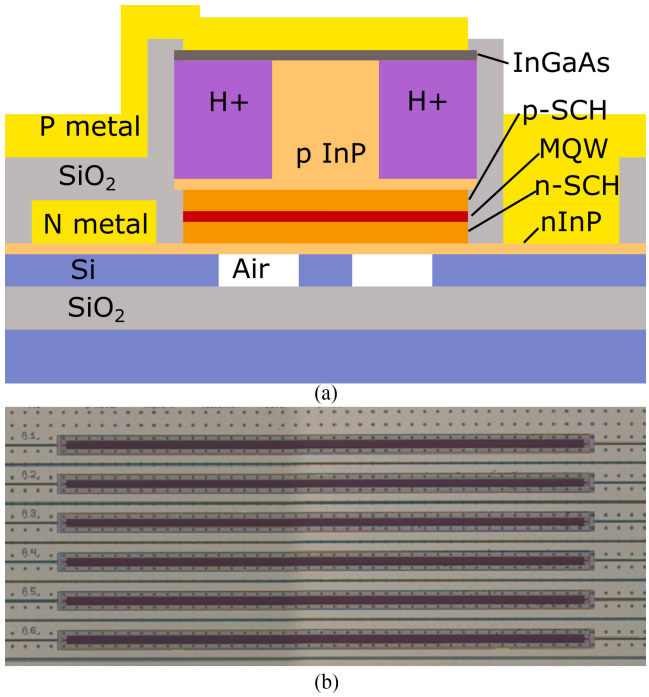

Fig. 2. (a) Schematic cross section of a directly bonded heterogeneous waveguide with a wide implanted mesa design. (b) Micrograph of the fabricated amplifiers prior to metallization.

The amplifiers demonstrated in this paper use the same quantum well and barrier design as in [22], with the number of wells reduced from 8 to 3 in order to increase the saturation power [29]. A cross section of the heterogeneous amplifier waveguide is shown in Fig. 2a, and a plan view of the fabricated amplifiers is shown in Fig. 2b. The number of wells does not explicitly affect P_s, but the amplifier can be operated at higher carrier density. Because the maximum drive current is limited by device self-heating, two identical amplifiers with different number of quantum wells can operate at the same maximum current. This results in the lower number of wells operating at higher carrier density N, which decreases the differential gain and the carrier lifetime. From (3), this increases P_s.

The addition of the Si waveguide presents the advantage of allowing control of the confinement factor by varying the width of the Si ridge, as the effective index of this portion of the waveguide increases relative to the effective index of the III-V waveguide. This allows integration of low and high confinement factor waveguide sections on a single chip, enabling the combination of high gain and high saturation power amplifiers with low-threshold lasers. Decreasing the confinement factor in the III-V layers will also decrease the propagation loss, as the mode overlap increases with the low-doped Si. Low doped silicon typically has very low absorption. This allows integration with high slope efficiency lasers.

However, the proximity of the Si, which has relatively high refractive index compared to most InP alloys, requires special consideration. If the indices and thicknesses of the III-V layers are too low, it requires a very narrow or thin Si layer. This increases the scattering loss due to the narrow Si waveguide.

TABLE I
RELEVANT PROPERTIES OF THE HETEROGENEOUS WAVEGUIDE

Layer	Material	Thickness (nm)	Doping (cm^{-3})	Band Gap Wavelength (μm)	Strain[a]	Refractive Index	α (cm^{-1})
1	$In_{0.53}Ga_{0.47}As$	200	$p\,10^{19}$	1.65	0	3.7	10,000
2	InP	1000	$p\,1.5\cdot10^{18}$	0.92	0	3.17	33
3	InP	250	$p\,8\cdot10^{17}$	0.92	0	3.17	17.6
4	InP	250	$p\,5\cdot10^{17}$	0.92	0	3.17	5.5
5	$In_{0.53}Al_{0.18}Ga_{0.29}As$	125	$p\,1\cdot10^{17}$	1.20	0	3.38	1.1
6	3x $In_{0.65}Al_{0.06}Ga_{0.29}As$	7	u.i.d.	1.70	$+0.85\%$	3.41	83[b]
	4x $In_{0.45}Al_{0.09}Ga_{0.46}As$	10	u.i.d.	1.35	-0.55%		c
7	$In_{0.53}Al_{0.18}Ga_{0.287}As$	125	n 1 10^{17}	1.20	0	3.38	0.1
8	InP	110	n 1 $\cdot$ 10^{18}	0.92	0	3.17	1.0
9	2x $In_{0.85}Ga_{0.15}As_{0.33}P_{0.67}$ 2x InP	7.5	n 1 $\cdot$ 10^{18} n 1 $\cdot$ 10^{18}	1.110.92	00	3.283.17	1.0
10	InP	10	n 1 $\cdot$ 10^{18}	0.92	0	10	1.0
11	Bonding SiO_2	7	N/A	N/A	0	1.45	0
12	Si	500	u.i.d.	1.10	0	3.47	0
13	Buried SiO_2	1000	N/A	N/A	0	1.45	0

[a]Positive indicates compressive, negative indicates tensile.
[b]This value depends on the carrier density; this is under high injection current (280 mA).
[c]Loss from the barrier is contained in the loss value used for the well.

Balancing the size of the two waveguides is critical for ensuring high performance.

The design presented here was carried out by numerical simulation of the transverse optical mode in the gain region waveguide. The confinement factor Γ_{xy} and modal internal propagation loss α_i can be extracted from this simulation. Both values vary as a function of waveguide width. These can be used with a known or assumed material gain value to compute the net modal gain coefficient, g_{net},:

$$g_{net}(w) = \Gamma_{xy}(w) g_{p,0} - \alpha_i. \tag{4}$$

A value of 1650 cm^{-1} was used for material gain $g_{p,0}$, which was extrapolated based on small-signal measurements of Fabry-Perot lasers. Loss values are computed based on known relationships between the doping level and the absorption in InP [30]–[32]. There is some disagreement in literature [33], [34] on the absorption level in the quantum well. Using the value from [33], and calculating the carrier density [28] based on (5):

$$N = \sqrt{\frac{J\eta_i}{qN_w t_w B}}, \tag{5}$$

while assuming $J = 3400$ A/ cm^2 for the current density, $\eta_i = 0.6$ for the injection efficiency, knowing the thickness of the well $t_w = 7$ nm and the number of wells $N_w = 3$ from Table I, and $B = 10 \cdot 10^{-10}$ cm^3/ s for the bimolecular recombination rate, the absorption coefficient in the quantum well is calculated to be 83 cm^{-1}.

The real refractive indices are calculated using [35] for AlGaInAs and [36] for InGaAsP. The refractive index for the quantum well and barrier, which are not lattice matched to the substrate, was inferred by comparing measured mode width values to simulations. The net modal gain for a variety of SCH thicknesses versus Si waveguide width is shown in Fig. 3. The SCH thickness refers to the individual thickness of both the p-SCH and the n-SCH. For example, "125 nm SCH thickness" means that the p-SCH and the n-SCH are each 125 nm thick.

TABLE II
COMPARISON OF HETEROGENEOUS SOAS

First author	Year	G_0 (dB)	$P_{s,out}$ (dBm)	Type
H. Park	2007	13	8	Direct bond, implanted mesa[a]
H. Park	2007	9.5	—	Direct bond, implanted mesa
S. Keyvaninia	2012	13	—	BCB bond, narrow mesa
P. Kaspar	2015	28	9	Oxide bond, narrow mesa
S Cheung	2015	7.5	—	Direct bond, implanted mesa
This work	2016	25.5	12.3	Direct bond, implanted mesa
This work	2016	14.1	16.8	Direct bond, implanted mesa
ThorLabs[b]	2016	30	18	InP substrate

[a]No heterogeneous transition.
[b]Native InP substrate device, not integrated with silicon photonics. Available commercially through ThorLabs, part number BOA1007C

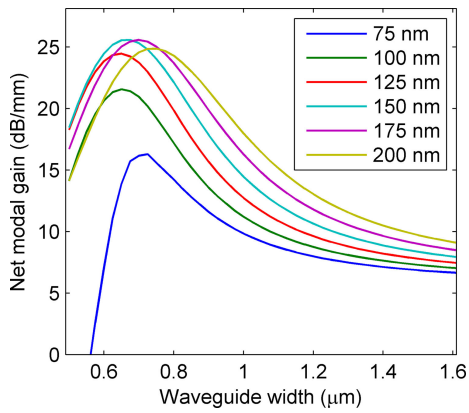

Fig. 3. Simulated net modal gain as a function of silicon waveguide width, for various thicknesses of the SCH.

It can be seen from Fig. 3 that the net modal gain increases with increasing SCH thickness, up to 175 nm. This is despite the decrease in quantum well confinement factor Γ_{xy}, which is shown in Fig. 4, after 125 nm. Thicker SCH layers pull the mode up into the III-V mesa, increasing maximum attainable Γ_{xy} up to a thickness of 125 nm, after which Γ_{xy} declines as the mode expands vertically into the SCH and out of the quantum

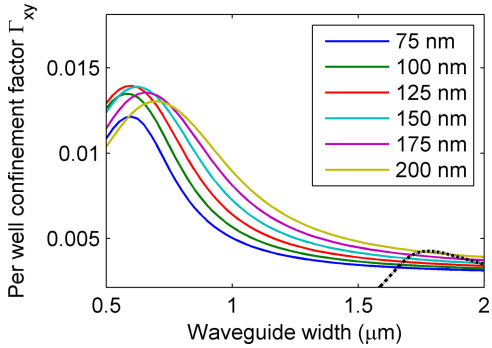

Fig. 4. Variation in the quantum well confinement factor versus waveguide width for various SCH thicknesses. The confinement factor for the first higher-order mode in the 125 nm SCH is shown as a black dotted line.

wells. Fig. 4 also shows the confinement factor of the first higher order mode (black dotted line, only 125 nm SCH thickness is shown for the higher order mode), which limits the minimum confinement factor as the higher order mode begins to compete for gain with the fundamental mode.

The deterioration in the net modal gain displayed by the thinner SCH curves is explainable by the propagation loss. The principal sources of loss in thin SCH waveguides are overlap with regions containing high density of holes, such as the p-doped InP cladding layers and the quantum wells, and band-to-band absorption in the InGaAs contact layer, which has a band gap of 1.65 μm. Another source of loss in directly bonded heterogeneous amplifiers that must be considered is mode leakage into the nearby Si slab. In order to preserve yield in directly bonded devices, the Si waveguide is formed by etching trenches into the device layer of the SOI wafer, so that the majority of the surface is planar Si to support the bonded film. This trench width is 3 μm in these devices.

Because the III-V mesa is wide and does not provide lateral index guiding with respect to the pumped region, very narrow Si waveguides can form leaky waveguides that couple with radiation modes in the Si slab. This phenomenon is indicated by the oscillating field outside of the waveguide core in Fig. 5a, which has a narrow 500 nm waveguide and thin 75 nm SCH layers, and has, according to the blue curve in Fig. 3, poor overall performance. Fig. 5b shows an 850 nm wide Si waveguide with 200 nm SCH layers, which shows less overlap with the lossy upper p-InP cladding and InGaAs contact, but still has evidence of radiation loss into the slab. Fig. 5c shows an intermediate SCH thickness, 125 nm, with a Si waveguide width of 850 nm, near the optimum performance. The mode is compact with little overlap with the upper section of the mesa and no evidence of radiation loss. Fig. 5d shows the structure without the optical mode overlay so that the structure and index of the waveguide is clearly visible.

The contributions to the loss vary depending on the geometry of the waveguide. For narrow Si waveguides, where the confinement factor is potentially high, the loss is dominated by absorption due to overlap with p-type doped layers and the InGaAs contact layer because the mode is weakly confined to the SCH region (Fig. 6a). For thick SCH layers, the loss is dominated by radiation into the Si (Fig. 6b). Intermediate 125–175 nm SCH thicknesses have a balance between the two (Fig. 6c).

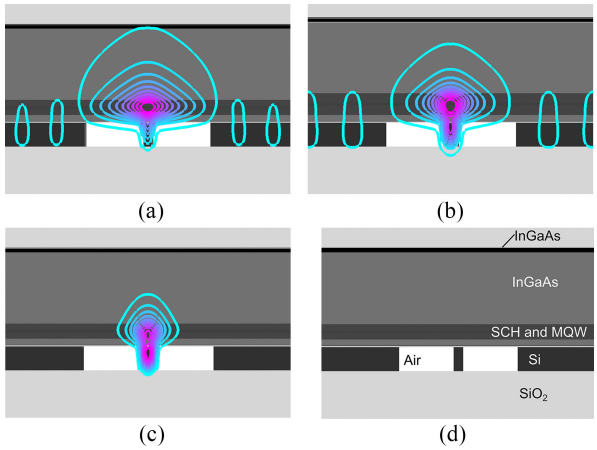

Fig. 5. TE polarized electric field profile (colored contours) superimposed over the refractive index profile (grayscale). Darker colors indicate higher index. (a) A narrow 500 nm silicon waveguide with thin 75 nm SCH layers, showing radiation loss and overlap with the InGaAs contact. (b) An 850 nm silicon waveguide with thick 200 nm SCH layers, showing only radiation loss. (c) An 850 nm silicon waveguide with 125 nm SCH layers, showing little overlap with the InGaAs and no radiation loss. (d) Index profile only, for the purpose of illustration.

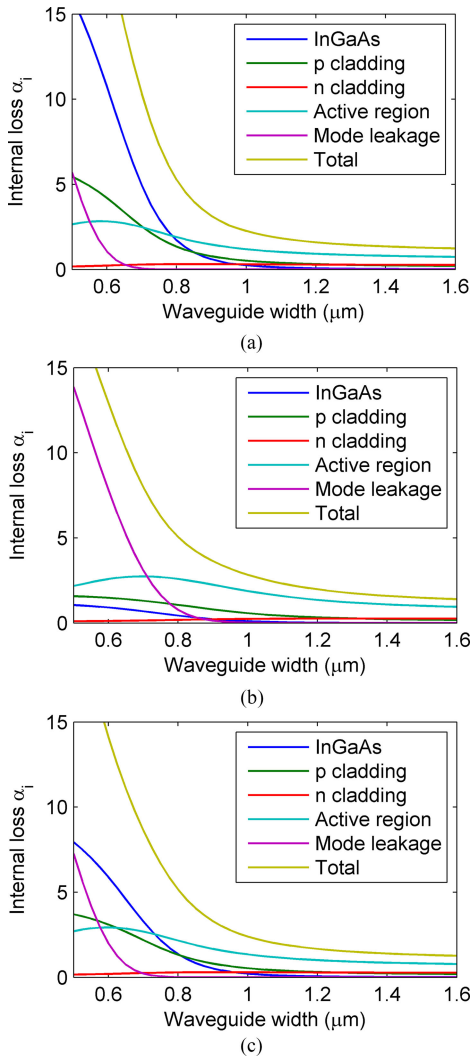

Fig. 6. Loss contributions from the various III-V layers for (a) 75 nm SCH, (b) 200 nm SCH, and (c) 125 nm SCH.

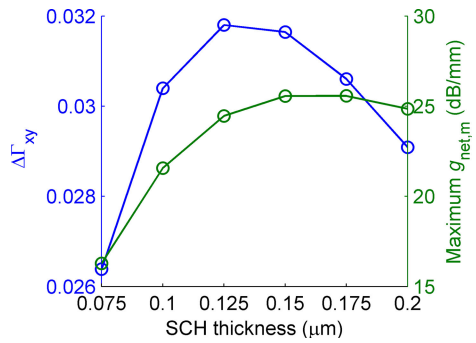

Fig. 7. Maximum attainable difference between quantum well confinement factor, on the left axis, and maximum net modal gain on the right axis, versus SCH thickness.

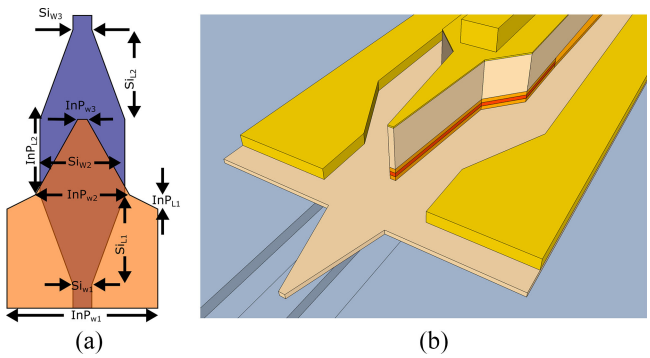

Fig. 8. (a) Schematic view of the Si/III-V transition. The III-V mesa is in orange, with the underlying silicon waveguide in blue. The dimensions are listed in Table III. (b) Isometric view of the completed taper, with silicon in blue, InP in beige, SCH in orange, MQW in red, and contact metal in yellow. Neither drawing is to scale.

Although the loss is ultimately lower for thicker SCH layers, the reduced confinement factor renders lower net modal gain compared to intermediate thickness. Another factor to consider is $\Delta\Gamma_{\mathrm{xy}}$, the potential difference in confinement factor attainable by differing the waveguide width, and is shown in Fig. 7, along with the maximum g_{net} for whichever waveguide width has the highest value. Si waveguide widths beyond 1.6 μm support a higher-order TE_{10} transverse mode, so that value represents the width with the minimum confinement factor. For integration of high gain SOAs with high power SOAs, $\Delta\Gamma_{\mathrm{xy}}$ and g_{net} should be maximized. For this reason, 125 nm thick SCH layers were chosen for these devices.

It is possible that further optimization could continue to improve the performance. For example, reducing the thickness of the InGaAs layer to 50 nm would reduce the loss at 0.6 μm waveguide width and 125 nm SCH by 6 cm^{-1}, and increasing the thickness of the low-doped p-InP cladding would shift the optimum g_{net} toward thinner SCH layers and thinner Si waveguides. An increase in the width of the current channel would reduce the confinement factor roll off as the waveguide size decreased. The introduction of a transparent p-contact such as indium tin oxide, or one with lower real index of refraction, may eliminate the p-contact as a source of loss. This would only represent an improvement if sufficiently low electrical resistance could be attained. The technique has been used successfully with gallium-nitride-based visible wavelength lasers [37].

IV. III-V to Si Transition

Heterogeneous Si/III-V components typically require a transition from the active heterogeneous waveguide into a passive Si waveguide. This transition is required for integration with passive Si devices such as arrayed waveguide gratings [38], distributed Bragg reflectors [39], or other III-V devices that require different epitaxial structures, such as photodetectors [40]. For an SOA, the transition should have insertion loss and reflection as low as possible, and bandwidth as high as possible. Insertion loss will directly reduce the gain and output power, while reflection will increase undesirable gain ripple and will cause high gain amplifiers to lase if the reflection is large enough. A transition with limited bandwidth, such as a directional coupler or higher-order Bragg grating, will limit the bandwidth of the SOA.

TABLE III
Dimensions of III-V to Si Transition

Dimension	Size (μm)
$\mathrm{Si_{w1}}$	varies
$\mathrm{Si_{w2}}$	2
$\mathrm{Si_{w3}}$	0.8
$\mathrm{Si_{L1}}$	100
$\mathrm{Si_{L2}}$	100
$\mathrm{InP_{w1}}$	26
$\mathrm{InP_{w2}}$	4
$\mathrm{InP_{w3}}$	0.5*
$\mathrm{InP_{L1}}$	4

*This is the width of the InP p-cladding. The width of the wet etched undercut active region taper is $\sim$ 150 nm.

Lateral tapers have the potential to fulfill all of these requirements. If the transition is sufficiently gradual, loss may be minimized. Since there is no resonance or phase matching condition, an adiabatic lateral taper can have low loss over a wide range of wavelengths. The reflection depends on the width of the taper at termination. The III-V/Si transition used in this work is based on the design in [23], and is shown schematically in Fig. 8. The operating principle is as follows: The Si waveguide inside the active region tapers from the width of the waveguide in the active region, Si_{w1}, to a very wide width, Si_{w2}, in order to decrease confinement in the III-V layers. The wide III-V mesa is then rapidly reduced in width from 26 μm to 4 μm, before tapering more gradually to 0.5 μm. The width of $\mathrm{InP_{w3}}$ is at the base of the mesa, and is limited by the verticality of the mesa dry etch. In order to reduce reflection, the SCH and MQW layers were wet etched, undercutting the InP mesa and creating a very sharp tip. The Si waveguide is then tapered down to a smaller, single-mode waveguide for bends and passive circuitry.

Similar designs have shown losses below 0.5 dB and reflection below 45 dB in [23] and [41]. However, neither measurement method in those references included absorption loss in the taper QWs, and it was found in [42] that laser threshold and lasing wavelength increased as the length of the taper increased, suggesting absorption.

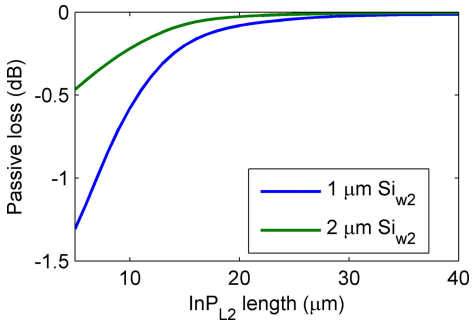

Fig. 9. Simulated passive transmission loss through the InP taper, for varying widths of the wide silicon waveguide underneath.

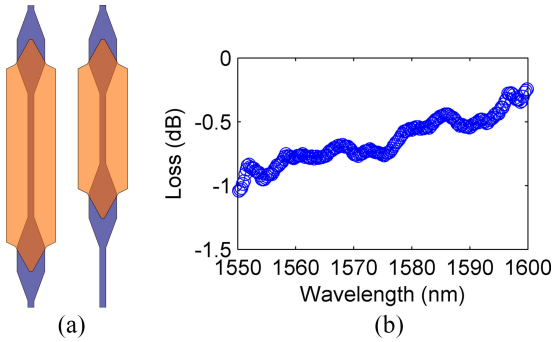

Fig. 10. (a) Schematic of the two devices used for the taper loss measurement (b) Loss versus wavelength from a single tapered mode converter.

It is likely that the narrow taper structure has increased resistance due to hydrogen passivation of the p-type dopant introduced by plasma processing, specifically the methane-hydrogen-argon (MHA) dry etch used to form the III-V mesa [43]–[45]. The InP taper is then pumped at a lower current density, which red-shifts the emission spectrum relative to the amplifier waveguide section. The hydrogen passivation effect in InP can normally be mostly corrected with rapid thermal annealing. Unfortunately, bonded films of InP are more sensitive to high temperatures, and annealing sufficient to re-activate the p-dopant after exposure to hydrogen plasma degrades the optical performance of the amplifier.

The impact of the absorption can be mitigated by reducing the length of the InP taper. This is achieved by using a wide Si waveguide underneath the InP taper, reducing the overlap with the III-V layers and thereby reducing the required length, as shown in Fig. 9. Passive loss due to the short taper is below 0.1 dB at 20 μm of length and a 2-μm-wide Si waveguide underneath. This analysis does not include scattering loss, which is considered to be minimal due to the smooth sidewall typically achieved by MHA etching [46].

In order to characterize the loss in the taper under forward bias and inside a working amplifier structure, a pair of 3-section lasers with identical design with the exception of the gain section length were devised, shown schematically in Fig. 10a. The lengths of the active regions, not including the taper, were $L_1 = 800$ μm and $L_2 = 1200$ μm. Both devices have polished Si facets with power reflectivity of $R = 0.28$. Each laser was biased below threshold at the same current density, 620 A/ cm^2, or 16 mA and 20 mA, respectively. The spectral gain was measured using an optical spectrum analyzer and the mode-sum minimum method [47]. Neglecting device heating, which should be minimal at this current density, one can assume that the spectral gain should have similar peak wavelength and bandwidth, with the smaller laser producing less gain proportionally to L_1/L_2. Any difference must be ascribed to fixed losses inside the cavity because fiber-to-chip coupling loss is ignored in the calculation of gain using this method. Only the spectral shape of the Fabry-Perot modes is required. In this case the dominant source of fixed loss is the taper loss l_t. Using:

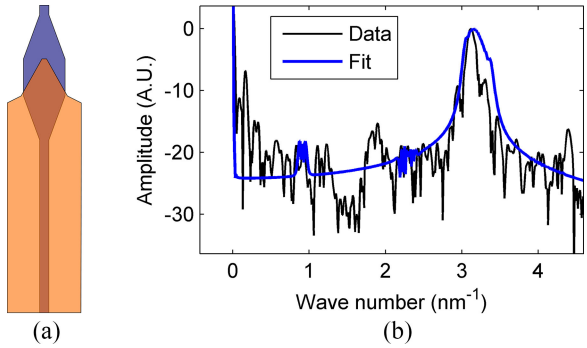

Fig. 11. (a) Schematic of the two-section laser used in the taper reflection measurement. (b) Fourier transform of the spectrum.

$$l_t(\lambda) = \{[g_1(\lambda, J_b) - g_1(\lambda, J_b)]\,\Delta L - \alpha_{\mathrm{Si}}\}\,L_1 L_2, \quad (6)$$

where $g_1(\lambda, J_b)$ and $g_2(\lambda, J_b)$ are the net modal gain coefficients versus wavelength of device 1 and 2 at bias current density J_b and α_{Si} is the loss of the extra length of Si waveguide on the shorter device. The Si waveguide loss must be captured with a separate measurement. In this case it was only 0.02 dB over the length of 400 μm. The result of the calculation can be seen in Fig. 10b. The taper has loss as low as 0.25 dB/taper at 1600 nm wavelength, but the loss increases to 1 dB at 1550 nm. The increasing loss as the wavelength decreases is believed to be due to absorption caused by unequal pumping of the taper versus the gain section. This increases the loss at 1550 nm to 1 dB/taper. Using a different etch chemistry that does not contain hydrogen, for example $Cl_2/N_2/Ar$ dry etch, may improve the loss at 1550 nm.

The reflection from the taper tip was measured using the method described in [41], only in this case the sub-threshold amplified spontaneous emission (ASE) spectrum was analyzed instead of the transmission spectrum. A two-section laser was prepared by dicing a three-section laser in half and polishing a heterogeneous facet in the middle, as shown in Fig. 11a. After collecting the optical spectrum of the device while biased at the waveguide transparency current $J_{tr,w}$, where $g_{\mathrm{net}} = 0$, the power spectrum was converted to the wave number domain with a Fourier transform to display the spatial frequencies of the cavity modes from the optical spectrum. A simple transmission matrix model of the laser cavity was then fit to the data using known length values for the unknown reflection at the taper tip.

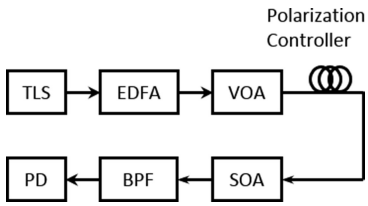

Fig. 12. The measurement apparatus used for the characterization of the gain and saturation power. TLS: Tunable laser source. EDFA: Erbium doped fiber amplifier. VOA: Variable optical attenuator. SOA: Semiconductor optical amplifier. BPF: Band pass filter. PD: Photodetector.

The fitted value for the field reflectivity is near the noise floor of the measurement, $r = 1 \cdot 10^{-3}$. There are two spectral features in the data that do not appear in the model. The peak at 0.2 nm^{-1} corresponds to the beat period between the TE_{00} and TE_{01} modes in the Si waveguide. A consequence of the short III-V taper is the generation of a small amount of the TE_{01} mode at the end of the transition. This accumulates a phase difference after propagating along the passive Si waveguide and reflecting off the Si facet, and interferes with the TE_{00} mode after recombining with it at the taper tip.

This spectral disturbance can be eliminated by using a shallowly etched waveguide that does not support a TE_{01} mode, or by increasing the length of the taper to 40 μm, at the cost of increasing the loss due to absorption. The cause of the broad peak at 2 nm^{-1} is unknown; however, it is unrelated to the taper, as it is present in pure, single-section Fabry-Perot cavity lasers that do not have a taper.

V. Experimental Results

Characterization of the SOA gain and saturation power was performed under continuous wave illumination by injecting light from a single-wavelength laser into the device with a tapered fiber, then measuring the output power of the SOA as the input power from the laser was varied. Due to the high coupling loss between the fiber and the facet (9 dB/facet), an erbium-doped fiber amplifier (EDFA) was used to ensure that the input power was high enough to saturate all of the SOA designs. The laser power after amplification by the EDFA was controlled with a variable optical attenuator. Because the SOA has compressively-strained quantum wells, it has the highest gain for TE polarized light. A fiber spool polarization controller was used to adjust the polarization of the input light. After the SOA, a band-pass filter was used to filter out ASE, to prevent it from being counted as signal power at low input levels. The light was finally collected on a photodetector. A schematic of the measurement apparatus is shown in Fig. 12.

The characterization of the gain versus input power for extraction of the gain saturation behavior was performed at 1.55 μm, where the gain was at its maximum. All of the measurements were performed with 280 mA of bias current. The operating voltage at this bias value was 2.3 V. The variation of the gain with respect to input power is shown in Fig. 13.

Using (1) and (7) to fit the measurement data, the unsaturated gain G_0 and saturation power P_s were extracted from each

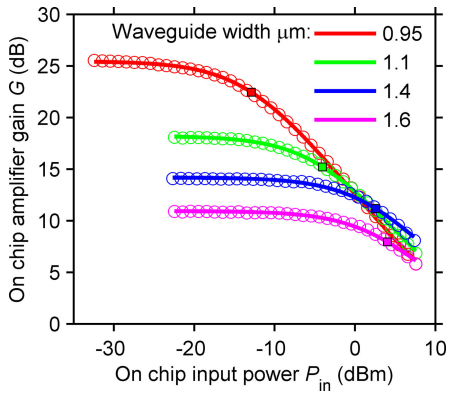

Fig. 13. Gain versus on-chip input power for all four SOA designs. The measurement data is shown as circles, and curve fits are shown as lines. The 3 dB saturation points are shown as squares.

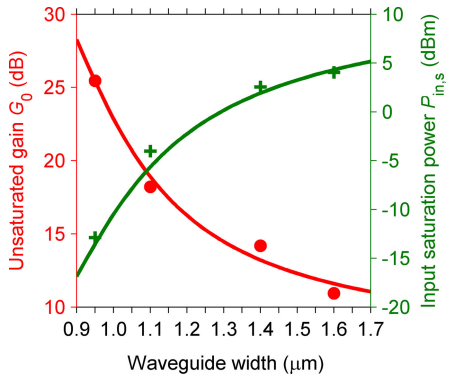

Fig. 14. Unsaturated gain G_0 (red) and input saturation power $p_{\mathrm{in},s}$ (green) extracted from the data in Fig. 13 (markers), and curve fits (lines).

device design. The fit parameters are shown versus waveguide width in Fig. 14.

The trend lines are fits to equations (7) for the unsaturated gain and (3) for the input saturation power.

$$G_0 = \exp(g_{p,0} L \Gamma_{\mathrm{xy}}). \tag{7}$$

where $L = 2$ mm is the gain section length. The peak gain parameter $g_{p,0}$ is used to fit the data, and in this case $g_{p,0} = 1.49 \cdot 10^3$ cm^{-1}. Equation (7) is only valid in the case where the net modal gain is much larger than the internal loss, as is often the case in an SOA with very high forward bias.

The spectral bandwidth of the amplifier was also tested. Because S- and L-band EDFAs with high enough output power were not available, this test was performed in the small signal regime with –12 dBm input power. The wavelength spectra of the various SOA designs were similar, so only the data from the 1.4 μm waveguide SOA is shown, in Fig. 15. The device achieved 30 nm of 1 dB bandwidth and 66 nm of 3 dB bandwidth. The data are shown as dots, while the red line is a curve fit using:

$$G \propto \exp[-\Gamma_{\mathrm{xy}} a_2 L (\lambda - \lambda_p)^2]. \tag{8}$$

where the constant a_2 is the spectral gain coefficient from [48], and is 31 cm^{-1}·nm^{-2} in this case.

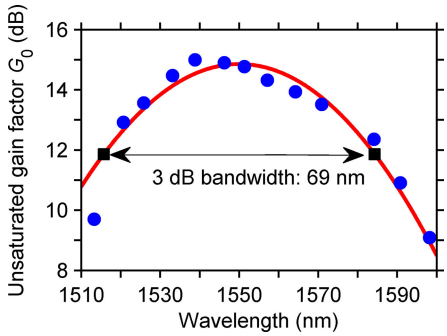

Fig. 15. Unsaturated gain G_0 versus wavelength for the 1.4 μm device under 280 mA bias current. The blue circles are data, while the red line is the curve fit using (8).

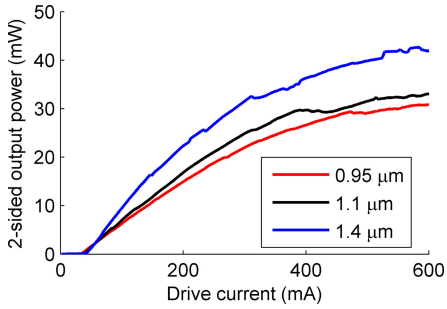

Fig. 16. Output power versus drive for various waveguide widths.

In addition to demonstrating high gain and high saturation power, the amplifiers are capable of producing high performance lasers. Prior to AR coating, the devices lase due to the 0.28% power reflection from the polished Si facets. The light-current characteristics of the 0.95, 1.1, and 1.4 μm waveguide devices before coating were measured from both sides of the device using an integrating sphere as it was operating as a laser, shown in Fig. 16.

Variation in the laser threshold current $I_{\rm th}$ is due to the increasing confinement factor as the Si waveguide width is narrowed (Fig. 4), which decreases the gain threshold. The variation in slope efficiency is caused by increasing internal loss as the waveguide width is narrowed, as shown in Fig. 6c. The maximum power of the 1.4 μm device is over 40 mW, or 16 dBm. The threshold is fairly high even for the best design, at 33 mA, but this is due to the high transparency current of the 2 mm long amplifier section. In terms of threshold current density, the device is quite outstanding at 403 kA/ cm^2. It is possible that an optimized gain section length and cavity mirror combination could produce a much lower threshold current for a high efficiency laser. The slope efficiency, and thus the eventual maximum output power, is limited by the taper loss. At the lasing wavelength (1565 nm), the taper loss is 0.75 dB/taper. Calculations suggest that reducing or eliminating the taper loss could increase the slope efficiency by nearly a factor of 1.5. The 1.6 μm waveguide lases in a higher order transverse mode, which explains the drop in threshold current $I_{\rm th}$ and reduction in slope efficiency. The performance of the various devices is summarized in Table IV.

TABLE IV
SUMMARY OF MEASUREMENT RESULTS

W (μm)	G_0 (dB)	$P_{{\rm in},s}$ (dBm)	P_s (dBm)	$I_{\rm th}$ (mA)	*S.E.* (W/A)
0.95	25.45	–12.15	12.32	33.0	0.095
1.10	18.18	–3.88	14.17	37.6	0.12
1.40	14.14	2.95	16.75	41.9	0.15
1.60	10.91	4.31	14.50	34.8	0.048

Fit parameters for the four SOA designs, as well as the laser threshold and 2-sided slope efficiency of the devices before AR coating.

VI. CONCLUSION

Semiconductor optical amplifiers with high gain and high saturation power have been integrated on a single chip with low threshold current density and high output power lasers. Control of the confinement factor tradeoff between the gain and saturation power can be achieved by a lithography mask design only, as opposed to varying the physical composition of the epitaxial material. Unsaturated gain of 25.5 dB and input saturation power of 4.25 dBm were respectively demonstrated with the narrowest and with the widest waveguide SOA. These results were achieved with a 65-nm wide 3-dB gain bandwidth. One device showed 16.25 dBm of saturated output power, which is the highest that has been demonstrated in heterogeneous Si/III-V SOA. Careful waveguide design allowed for low propagation loss (<5 cm^{-1}) across a range of confinement factors ($1.2-2.6\%$) while ensuring single transverse mode operation. Selection of a three quantum well active region increases the carrier density, which improves P_s and increases the gain bandwidth. Very low parasitic reflection from the Si/III-V transition allows for operation of long amplifiers at high drive current, which increases the gain and saturation power. Because the input and output are both passive Si waveguides, these amplifiers can be seamlessly integrated with other heterogeneous Si/III-V devices. Examples include a power amplifier for a narrow-linewidth laser, a channel amplifier for an optical phased array beam steering chip, or a high-gain amplifier for an integrated photodetector.

Further increased performance from heterogeneous silicon SOAs is still possible. The gain and hence the ultimate output power in these devices was limited by self-heating due to series resistance in the diode p-contact, which was found through the transmission line method technique to be $2 \cdot 10^{-5}\,\Omega \cdot {\rm cm}^2$. This value could be reduced by an order of magnitude by optimizing the metallization procedure and increasing the doping level in the contact layer. The devices presented in this work have relatively low thermal impedance, due to the 26 μm wide III-V mesa which acts as a heat sink and has direct contact with the 500 nm silicon layer. Silicon is a reasonably good thermal conductor (130 K/W/m), and so the heat can spread laterally, overcoming the limitation on heat dissipation imposed by the buried oxide layer. The thermal impedance, measured with thermal reflectance microscopy, is 11 K/W, which is comparable to P-side up diodes on InP substrates. Packaging by flip-chip bonding the SOA to a heat sink is shown through numerical simulation to reduce the thermal impedance further, down to 6 K/W.

Lower resistance will allow higher drive current and thus higher gain and saturation power due to increased carrier density and reduced carrier lifetime. The addition of current blocking layers, such as an electron blocking layer or graded index SCH, would also allow for operation of the device at higher carrier density. A reduction in the number of quantum wells would also be helpful for increasing the saturation power, but this would come at the cost of increased footprint due to lower gain per unit length and a potential reduction in laser performance if the same epitaxial structure is used for integration with lasers.

ACKNOWLEDGMENT

M. L. Davenport woukd like to thanks J. Peters for assistance with fabrication of the amplifiers, and C. Zhang and A. Liu for helpful discussions.

REFERENCES

[1] C. R. Doerr, "Silicon photonic integration in telecommunications," *Front. Phys.*, vol. 3, pp. 1–16, Aug. 2015.
[2] M. J. R. Heck *et al.*, "Hybrid silicon photonic integrated circuit technology," *IEEE J. Sel. Topics Quantum Electron.*, vol. 19, no. 4, Jul./Aug. 2013, Art. no. 6100117.
[3] M. Smit, J. van der Tol, and M. Hill, "Moore's law in photonics," *Laser Photon. Rev*., vol. 6, no. 1, pp. 1–13, 2012.
[4] J. C. Hulme *et al.*, "Fully integrated hybrid silicon two dimensional beam scanner," *Opt. Express*, vol. 23, no. 5, pp. 5861–5874, 2015.
[5] M. Hochberg and T. Baehr-Jones, "Towards fabless silicon photonics," *Nature Photon.*, vol. 4, no. 8, pp. 492–494, 2010.
[6] H. Abediasl and H. Hashemi, "Monolithic optical phased-array transceiver in a standard SOI CMOS process," *Opt. Express*, vol. 23, no. 5, pp. 6509–6519, 2015.
[7] J. Sun, E. Timurdogan, A. Yaacobi, E. S. Hosseini, and M. R. Watts, "Large-scale nanophotonic phased array," *Nature*, vol. 493, no. 7431, pp. 195–199, 2013.
[8] V. W. S. Chan, "Free-space optical communications," *J. Lightwave Technol.*, vol. 24, no. 12, pp. 4750–4762, Dec. 2006.
[9] B. Mason, J. Barton, G. A. Fish, L. A. Coldren, and S. P. DenBaars, "Design of sampled grating DBR lasers with integrated semiconductor optical amplifiers," *IEEE Photon. Technol. Lett.*, vol. 12, no. 7, pp. 762–764, Jul. 2000.
[10] S. Murthy *et al.*, "Large-scale photonic integrated circuit transmitters with monolithically integrated semiconductor optical amplifiers," in *Proc. Opt. Fiber Commun./Nat. Fiber Opt. Engineers Conf.*, 2008, Paper OWE1.
[11] R. Nagarajan *et al.*, "Monolithic, 10 and 40 channel InP receiver photonic integrated circuits with on-chip amplification," in *Proc. Opt. Fiber Commun. Conf. Expo./Nat. Fiber Opt. Engineers Conf.*, 2007, pp. 40–42.
[12] T. Durhuus, B. Mikkelsen, C. Joergensen, S. L. Danielsen, and K. E. Stubkjaer, "All-optical wavelength conversion by semiconductor optical amplifiers," *J. Lightwave Technol.*, vol. 14, no. 6, pp. 942–954, Jun. 1996.
[13] G.-H. Duan *et al.*, "Hybrid III–V on silicon lasers for photonic integrated circuits on silicon," *Proc. SPIE*, vol. 9002, no. 4, 2014, Art. no. 90020X.
[14] A. R. Hawkins, W. Wu, P. Abraham, K. Streubel, and J. E. Bowers, "High gain-bandwidth-product silicon heterointerface photodetector," *Appl. Phys. Lett.*, vol. 70, no. 1997, pp. 303–305, 1997.
[15] D. Liang *et al.*, "Uniformity study of wafer-scale InP-to-silicon hybrid integration," *Appl. Phys. A Mater. Sci. Process.*, vol. 103, no. 1, pp. 213–218, 2011.
[16] S. Keyvaninia *et al.*, "Ultra-thin DVS-BCB adhesive bonding of III-V wafers, dies and multiple dies to a patterned silicon-on-insulator substrate," *Opt. Mater. Express*, vol. 3, no. 1, pp. 35–46, 2013.
[17] S. Matsuo *et al.*, "Directly modulated buried heterostructure DFB laser on SiO_2/Si substrate fabricated by regrowth of InP using bonded active layer," *Opt. Express*, vol. 22, no. 10, pp. 12139–12147, 2014.
[18] H. Boudinov, H. H. Tan, and C. Jagadish, "Electrical isolation of n-type and p-type InP layers by proton bombardment," *J. Appl. Phys.*, vol. 89, no. 10, pp. 5343–5347, 2001.
[19] M. N. Sysak *et al.*, "Experimental and theoretical thermal analysis of a hybrid silicon evanescent laser," *Opt. Express*, vol. 15, no. 23, pp. 15041–15046, 2007.
[20] P. Kaspar *et al.*, "Hybrid III–V/Silicon SOA in optical network based on advanced modulation formats," *IEEE Photon. Technol. Lett.*, vol. 27, no. 22, pp. 2383–2386, Nov. 2015.
[21] S. Keyvaninia *et al.*, "III–V-on-silicon anti-colliding pulse-type mode-locked laser," *Opt. Lett.*, vol. 40, no. 13, pp. 3057–3060, 2015.
[22] H. Park *et al.*, "A hybrid AlGaInAs-silicon evanescent amplifier," *IEEE Photon. Technol. Lett.*, vol. 19, no. 4, pp. 230–232, Feb. 2007.
[23] H. Park *et al.*, "A hybrid AlGaInAs-silicon evanescent preamplifier and photodetector," *Opt. Express*, vol. 15, no. 21, pp. 13539–13546, 2007.
[24] S. Keyvaninia *et al.*, "A highly efficient electrically pumped optical amplifier integrated on a SOI waveguide circuit," in *Proc. IEEE 9th Int. Conf. Group IV Photon.*, 2012, vol. 6, pp. 222–224.
[25] A. Yariv and X. Sun, "Supermode Si/III-V hybrid lasers, optical amplifiers and modulators: A proposal and analysis," *Opt. Express*, vol. 15, no. 15, pp. 9147–9151, 2007.
[26] B. Ben Bakir *et al.*, "Electrically driven hybrid Si/III-V lasers based on adiabatic mode transformers," in *Proc. SPIE*, vol. 7719, 2010, pp. 77191F–77191F–9.
[27] S. Cheung, Y. Kawakita, K. Shang, and S. J. Ben Yoo, "Highly efficient chip-scale III-V/silicon hybrid optical amplifiers," *Opt. Express*, vol. 23, no. 17, pp. 22431–22443, 2015.
[28] L. A. Coldren and S. W. Corzine, "Diode lasers and photonic integrated circuits," *Opt. Eng.*, vol. 36, no. 2, pp. 616–617, 1997.
[29] K. Morito, S. Tanaka, S. Tomabechi, and A. Kuramata, "A broad-band MQW semiconductor optical amplifier with high saturation output power and low noise figure," *IEEE Photon. Technol. Lett.*, vol. 17, no. 5, pp. 974–976, May 2005.
[30] H. C. Casey and P. L. Carter, "Variation of intervalence band absorption with hole concentration in p-type InP," *Appl. Phys. Lett.*, vol. 44, no. 1, pp. 82–83, 1984.
[31] J. D. Robert and E. Kapon, "Low-loss III-V semiconductor optical waveguides," *IEEE J. Quantum Electron.*, vol. 27, no. 3, pp. 626–640, Mar. 1991.
[32] M. S. Alam, M. S. Rahman, M. R. Islam, A. G. Bhuiyan, and M. Yamada, "Refractive index, absorption coefficient, and photoelastic constant: Key parameters of InGaAs material relevant to InGaAs-based device performance," in *Proc. IEEE 19th Int. Conf. Indium Phosphide Relat. Mater.*, May 2007, pp. 343–346.
[33] S. Kakimoto, "Intervalence band absorption loss coefficients of the active layer for InGaAs/InGaAsP multiple quantum well laser diodes," *J. Appl. Phys.*, vol. 92, no. 11, pp. 6403–6407, 2002.
[34] G. Fuchs *et al.*, "Intervalence band absorption in strained and unstrained InGaAs multiple quantum well structures," *Appl. Phys. Lett.*, vol. 60, no. 2, pp. 231–233, 1992.
[35] C. Grasse *et al.*, "Empirical modeling of the refractive index for (AlGaIn) as lattice matched to InP," vol. 045018, 2010.
[36] M. Amiotti and G. Landgren, "Ellipsometric determination of thickness and refractive index at 1.3, 1.55, and 1.7 μm for $In_{(1-x)}Ga_xAs_yP_{(1-y)}$ films on InP," *J. Appl. Phys.*, vol. 73, pp. 2965–2971, Mar. 1993.
[37] A. Pourhashemi *et al.*, "High-power blue laser diodes with indium tin oxide cladding on semipolar ($20\bar{2}\bar{1}$) GaN substrates," *Appl. Phys. Lett.*, vol. 106, no. 11, p. 111105, 2015.
[38] G. Kurczveil *et al.*, "An integrated hybrid silicon multiwavelength AWG laser," *IEEE J. Sel. Topics Quantum Electron.*, vol. 17, no. 6, pp. 1521–1527, Nov. 2011.
[39] A. W. Fang *et al.*, "A distributed Bragg reflector silicon evanescent laser," *IEEE Photon. Technol. Lett.*, vol. 20, no. 20, pp. 1667–1669, Oct. 2008.
[40] H.-H. Chang, Y. Kuo, R. Jones, A. Barkai, and J. E. Bowers, "Integrated hybrid silicon triplexer," *Opt. Express*, vol. 18, no. 23, pp. 23891–23899, 2010.
[41] G. Kurczveil, P. Pintus, M. J. R. Heck, J. D. Peters, and J. E. Bowers, "Characterization of insertion loss and back reflection in passive hybrid silicon tapers," *IEEE Photon. J.*, vol. 5, no. 2, pp. 6600410–6600410, Apr. 2013.
[42] M. Davenport, M. Heck, and J. E. Bowers, "Characterization of a hybrid silicon-InP laser tapered mode converter," in *Proc. Cleo 2013*, 2013, Paper JTu4A.25.
[43] M. Moehrle, "Hydrogen passivation of Zn acceptors in InGaAs during reactive ion etching," *Esprit*, vol. 542, no. August 1989, pp. 542–544, 1990.
[44] J. Kreissl *et al.*, "Hydrogen passivation in InP:Zn resulting from reactive ion etching during laser stripe formation," in *Proc. 2000 Int. Conf. Indium Phosphide Relat. Mater.*, 2000, pp. 142–145.
[45] T. I. Gromova, E. I. Davydova, M. B. Uspenskii, and V. A. Shishkin, "SEM evidence for near-surface carrier passivation by hydrogen in CH_4/H_2 reactive ion etched p-InP.," *emicond. Sci. Technol.*, vol. 10, pp. 536–539, 1995.

[46] R. Grover, V. Hryniewicz, S. King, and V. Van, "Process development of methane–hydrogen–argon-based deep dry etching of InP for high aspect-ratio structures with vertical facet-quality sidewalls," *J. Vac. Sci. Technol. B, Microelectron. Nanometer Struct.*, vol. 19, pp. 1694–1698, 2001.
[47] D. T. Cassidy, "Technique for measurement of the gain spectra of semiconductor diode lasers," *J. Appl. Phys.*, vol. 56, no. 11, pp. 3096–3099, 1984.
[48] M. J. O'Mahony, "Semiconductor laser amplifiers for future fiber systems," *J. Lightwave Technol.*, vol. 6, no. 4, pp. 531–544, Apr. 1988.

Michael L. Davenport (S'10) received the Undergraduate degree in optical engineering from the University of Alabama Huntsville, Huntsville, AL, USA, in 2007 and the Master's degree in electrical engineering in 2009 from the University of California Santa Barbara, Santa Barbara, CA, USA, where he is currently working toward the Ph.D. degree in electrical engineering.

His research interests include low-noise single wavelength and mode-locked lasers for microwave photonics applications.

Sandra Skendžić received the Undergraduate and Master's degrees both in electrical engineering from the University of California, Santa Barbara, CA, USA, in 2013 and 2015, respectively.

Since July 2015, she has been an Optoelectronics Design Engineer with Ultra Communications, Inc., Vista, CA, USA.

Nicolas Volet received the Ph.D. degree in physics from École Polytechnique Fédérale de Lausanne, Lausanne, Switzerland, in 2014.

In 2008–2009, he worked on solar cells based on quantum confinement at the University of Houston. He developed a new technology for the optical mode control in long-wavelength vertical-cavity surface-emitting lasers. He also contributed for the understanding of the polarization properties of these devices, both theoretically and experimentally. In 2015, he received an Early Postdoc. He is currently a Postdoctoral Researcher at the University of California, Santa Barbara, CA, USA, where he works on photonics devices integrated on a silicon platform.

Dr. Volet received one-year scholarship at Carnegie Mellon University, Pittsburgh, PA, USA, in 2006–2007. He also received the Mobility Fellowship from the Swiss National Science Foundation.

Jared C. Hulme received the B.S. degree in electrical engineering from Brigham Young University, Provo, UT, USA, in 2008. He is currently working toward the Master's/Ph.D. degrees in electronics and photonics at the University of California, Santa Barbara, CA, USA.

His research interest is focused on heterogeneous III/V silicon ring-based tunable lasers and their applications in photonic integrated circuits. He has done work on the DARPA SWEEPER Project, which involves the integration of 164 components to create a two-dimensional beam-steering device with no moving parts. He is currently working in collaboration with Keysight to build a fully integrated photonic microwave generator.

Martijn J. R. Heck (S'04–M'09) received the M.Sc. degree in applied physics and the Ph.D. degree from the Eindhoven University of Technology, Eindhoven, The Netherlands, in 2002 and 2008, respectively.

He is an Associate Professor in the Department of Engineering, Aarhus University, Aarhus, Denmark, where he is involved in research on photonic integration technologies and applications. From 2007 to 2008, he was a Postdoctoral Researcher with the COBRA Research Institute, Eindhoven University of Technology, where he was engaged in the development of a technology platform for active–passive integration of photonic integrated circuits. From 2008 to 2009, he was with the Laser Centre, Vrije Universiteit, Amsterdam, The Netherlands, where he was involved in the development of integrated frequency-comb generators. From 2009 to 2013, he was a Postdoctoral Researcher and the Associate Director of the Silicon Photonics Center, University of California Santa Barbara, Santa Barbara, CA, where he was involved in research on photonic integrated circuits based on the heterogeneous integration of silicon, silica, and III/V photonics.

John E. Bowers (S'78–M'81–SM'85–F'93) received the M.S. and Ph.D. degrees from Stanford University, Stanford, CA, USA.

He was with AT& Bell Laboratories and Honeywell. He holds the Fred Kavli Chair in Nanotechnology, and is the Director of the Institute for Energy Efficiency and a Professor with the Departments of Electrical and Computer Engineering and Materials, University of California, Santa Barbara, CA, USA. He is the Cofounder of Aurrion, Aerius Photonics, and Calient Networks. He has authored ten book chapters, 600 journal papers, 900 conference papers, and holds 54 patents. His research interests include optoelectronics and photonic integrated circuits.

Dr. Bowers is a Member of the National Academy of Engineering and a Fellow of the OSA and the American Physical Society. He received the OSA/IEEE Tyndall Award, the OSA Holonyak Prize, the IEEE LEOS William Streifer Award, and the South Coast Business and Technology Entrepreneur of the Year Award. He and his coworkers received the EE Times Annual Creativity in Electronics Award for the most promising technology for the heterogeneous silicon laser in 2007.